Check for updates

RESEARCH ARTICLE

ADVANCED MATERIALS
www.advmat.de

Stainless Steel Activation for Efficient Alkaline Oxygen Evolution in Advanced Electrolyzers

Yong Zuo, Valentina Mastronardi, Agnese Gamberini, Marilena I. Zappia, Thi-Hong-Hanh Le, Mirko Prato, Silvia Dante, Sebastiano Bellani,* and Liberato Manna**

Designing robust and cost-effective electrocatalysts for efficient alkaline oxygen evolution reaction (OER) is of great significance in the field of water electrolysis. In this study, an electrochemical strategy to activate stainless steel (SS) electrodes for efficient OER is introduced. By cycling the SS electrode within a potential window that encompasses the Fe(II)↔Fe(III) process, its OER activity can be enhanced to a great extent compared to using a potential window that excludes this redox reaction, decreasing the overpotential at current density of 100 mA cm^{-2} by 40 mV. Electrochemical characterization, Inductively Coupled Plasma – Optical Emission Spectroscopy, and *operando* Raman measurements demonstrate that the Fe leaching at the SS surface can be accelerated through a Fe → γ-Fe_2O_3 → Fe_3O_4 or FeO → Fe^{2+} (aq.) conversion process, leading to the sustained exposure of Cr and Ni species. While Cr leaching occurs during its oxidation process, Ni species display higher resistance to leaching and gradually accumulate on the SS surface in the form of OER-active Fe-incorporated NiOOH species. Furthermore, a potential-pulse strategy is also introduced to regenerate the OER-activity of 316-type SS for stable OER, both in the three-electrode configuration (without performance decay after 300 h at 350 mA cm^{-2}) and in an alkaline water electrolyzer (≈30 mV cell voltage increase after accelerated stress test-AST). The AST-stabilized cell can still reach 1000 and 4000 mA cm^{-2} at cell voltages of 1.69 and 2.1 V, which makes it competitive with state-of-the-art electrolyzers based on ion-exchange membrane using Ir-based anodes.

1. Introduction

Water electrolysis powered by renewable electricity is a sustainable route to produce green hydrogen. Unlike the hydrogen evolution reaction (HER) occurring at the cathode of a water electrolyzer, the oxygen evolution reaction (OER) at the anode can be the kinetically limiting reaction, primarily due to the involvement of a higher number of electron transfers (four vs two).[1–3] Despite IrO_2 and RuO_2 representing efficient OER catalysts, their scarcity and high cost hinder their use in massive industrial scenarios.[4–6] Alternatively, nickel-iron (Ni-Fe)-based electrocatalysts have emerged as outstanding choices over the past decade, becoming the go-to catalysts for the OER in alkaline environments.[7–9]

Revealing the mechanisms of NiFe-catalyzed OER is a currently active research topic,[10,11] since it is still unclear whether Ni or Fe is the active site.[12–21] Nevertheless, consensus on various points has been reached: 1) NiOOH could serve as a suitable "host" for Fe^{3+} incorporation; 2) $Ni_{1-x}Fe_xOOH$ significantly outperforms the single components of NiOOH and FeOOH. Consequently, incorporating Fe into Ni-based electrocatalysts is an effective strategy for designing efficient catalysts for the OER.[14,19,20] Commercially available stainless steel (SS), containing both Fe and Ni, can intrinsically represent a promising OER catalyst candidate. Nevertheless, it has only recently been seriously considered for this role.[22,23] Previous efforts primarily focused on synthesizing electrodes using reagents as precursors to grow specific NiFe-based catalyst layers on substrates such as SS,[24] Cu,[25] Ni foams/felts,[26] etc. However, their durability came into question due to the potential detachment or leaching of the catalyst layer

---

Y. Zuo, T.-H.-H. Le, L. Manna
Nanochemistry Department
Istituto Italiano di Tecnologia
Via Morego 30, Genova 16163, Italy
E-mail: yong.zuo@iit.it; liberato.manna@iit.it

The ORCID identification number(s) for the author(s) of this article can be found under https://doi.org/10.1002/adma.202312071

© 2024 The Author(s). Advanced Materials published by Wiley-VCH GmbH. This is an open access article under the terms of the Creative Commons Attribution License, which permits use, distribution and reproduction in any medium, provided the original work is properly cited.

DOI: 10.1002/adma.202312071

V. Mastronardi, A. Gamberini, M. I. Zappia, S. Bellani
BeDimensional S.p.A.
Via Lungotorrente Secca
30R, Genova 16163, Italy
E-mail: s.bellani@bedimensional.it

T.-H.-H. Le
Dipartimento di Chimica e Chimica Industriale
Università di Genova
Genova 16146, Italy

M. Prato, S. Dante
Materials Characterization Facility
Istituto Italiano di Tecnologia
Via Morego 30, Genova 16163, Italy

Table 1. Properties of SS electrodes investigated in this work.

Anode	Wire diameter/ Thickness [mm]	Mesh number /Porosity [%]	Composition[a)] [atom %]				
			Fe	Ni	Cr	Mo	Mn
SSM316	0.14	80 mesh	69.88	9.90	19.10	1.12	/
SSM304	0.13	80 mesh	68.63	6.23	23.90	/	1.23
SSF316L	0.68	78%	69.37	10.54	18.91	1.18	/

[a)] Measured by SEM-EDS.

under harsh practical operating conditions. In this regard, SS electrodes can be considered as straightforward choices for the dynamic generation of a surface NiFe-based catalyst layer, derived from its bulk composition, while acting as porous transport layers to efficiently collect the evolved gases in practical electrolyzer configurations.[22,23]

Although the SS mesh (SSM) already exhibits superior OER activity compared to other commercially available electrodes like Ni foam/mesh[27–29] and Cu foam,[29] its performance is still unsatisfactory, e.g., requiring ≈350 mV to achieve a current density of 10 mA cm^{-2} in a 1 м NaOH.[28] Consequently, strategies have been proposed to enhance the activity of SSM toward alkaline OER. For instance, 316L-type SS plate has been activated in a concentrated LiOH electrolyte (5 м LiOH) through prolonged in situ OER operation, resulting in the formation of an active and stable surface thin catalyst layer.[30] Other treatments, such as anodization in a strongly alkaline medium at a high current density (e.g., ≈1800 mA cm^{-2})[31] and Cl_2-induced surface oxidation,[32] have been reported. A crucial aspect of utilizing SS as an OER catalyst in alkaline media is the dynamic regeneration of the surface Ni-enriched catalytic layer formed due to the corrosion of its underlying bulk alloy.

Based on these preliminary considerations, herein we rationally introduce an electrochemical strategy to efficiently activate the 316-type SSM (SSM316) for alkaline OER operations and unveil the activation mechanism behind it. Unlike the conventional cyclic voltammetry (CV) that in this case is limited to a small potential range (e.g., 0 to 1V$_{Hg/HgO}$), the use of a wider potential range encompassing the Fe(II)↔Fe(III) redox process can facilitate the Fe leaching at the SS surface. This, in turn, exposes more Ni species, which can be transformed into Fe-incorporating NiOOH, acting as efficient catalysts for the OER. Furthermore, we propose a simplified potential-pulse strategy to regenerate the OER activity of SSM316 electrode, ensuring long-term performance stability. Thus, the SSM316 electrode can consistently catalyze OER at an industrial-level current density (≈ 350 mA cm^{-2}) for over 300 h with no performance degradation, demonstrating a significant improvement compared to a ≈37% current density decay observed after 250 h of continuous operation. This activation strategy can be extended to 304-type SS meshes (SSM304) and 316L-type SS felt (SSF316L). When implemented in a single cell of an alkaline electrolyzer (AEL) based on a Pt/C cathode (0.4 mg$_{Pt}$ cm^{-2}), our activated SSM316-based anode emerges as the most performing one among the investigated SS electrodes, reaching 1000 and 4000 mA cm^{-2} at cell voltages of 1.69 and 2.1 V, respectively. These values are already competitive with those reached by state-of-the-art electrolyzers based on ion-exchange membrane.[33–35]

2. Results and Discussion

2.1. Electrochemical Characterizations and Analyses

Table 1 reports the geometrical properties and chemical composition (determined by scanning electron microscopy-energy dispersive spectroscopy -SEM-EDS) of the SS electrodes investigated in this work.

The CV-aided activation process was first evaluated on SSM316 using a potential scan rate of 5 mV s^{-1}. This step was conducted in a 1 м NaOH electrolyte at room temperature (RT, ≈20 °C), using a three-electrode configuration and evaluating three distinct potential windows (PWs), namely, 0–1 V$_{Hg/HgO}$ (PW1), −0.5–1 V$_{Hg/HgO}$ (PW2), and −1–1 V$_{Hg/HgO}$ (PW3).

As illustrated in Figure S1 (Supporting Information), the OER activity of the SSM316 gradually increased during the CV cycles in all cases, and almost stabilized after 15 cycles. **Figure** 1a presents the stabilized CV curves recorded at the 15th cycle for the three different PWs. SSM316 activated with the PW3 (hereafter referred to as SSM316_PW3) significantly outperformed those activated with the PW1 and PW2 (named SSM316_PW1 and SSM316_PW2, respectively). In fact, SSM316_PW3, regardless of whether it was initially scanned from −1 or 0 V$_{Hg/HgO}$, showed a much lower overpotential (by ≈40 mV) to reach 100 mA cm^{-2} after 15 CV cycles (Figure 1b). Conversely, SSM316_PW1 and SSM316_PW2 consistently demonstrated similar OER activities. Notably, unlike the fully activated SSM316_PW1 and SSM316_PW2, which exhibited the same color as the blank SSM316, SSM316_PW3 displayed a brownish color, indicating the formation of a different surface catalyst layer compared to the former cases. Furthermore, additional experiments revealed that the activity of SSM316_PW3 is not affected by the potential scan rate (Figure S2, Supporting Information). However, it requires more CV cycles to stabilize, i.e., ≈50 CV cycles at 50 mV s^{-1} (total duration: ≈66.7 min), while 15 CV cycles are needed at 5 mV s^{-1} (total duration: 200 min).

Focusing on the 15th CV profile measured on SSM316 at 5 mV s^{-1} potential scan rate, additional redox peaks become apparent in the potential range from −1 to −0.5 V$_{Hg/HgO}$, reached by the PW3, but not by PW1 and PW2 (see Figure 1c). Control experiments indicated that these redox peaks are associated with the Fe(II)↔Fe(III) conversion process at the SSM316 surface (Figure S3, Supporting Information). These results are consistent with previous literature.[36] Interestingly, while SSM316 activated using the three different PW ranges exhibit similar redox peaks associated to Ni(II)↔Ni(III) conversion process at ≈0.6 V$_{Hg/HgO}$ (oxidation) and 0.51 V$_{Hg/HgO}$ (reduction), SSM316_PW3 especially displays an additional broad oxidation peak at

© 2024 The Author(s). Advanced Materials published by Wiley-VCH GmbH

15214095, 2024, 21, Downloaded from https://onlinelibrary.wiley.com/doi/10.1002/adma.202312071 by Iit Istituto Italiano Di Tecnologia, Wiley Online Library on [27/09/2024]. See the Terms and Conditions (https://onlinelibrary.wiley.com/terms-and-conditions) on Wiley Online Library for rules of use; OA articles are governed by the applicable Creative Commons License

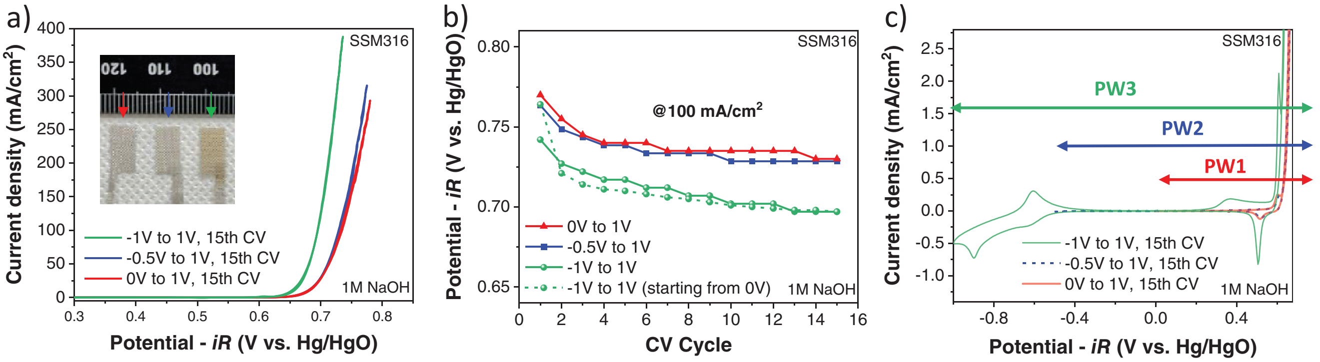

Figure 1. a) The CV curves recorded for SSM316 scanned in different PWs (PW1, PW2, PW3) at the 15th scan. The inset image shows the optical photograph of the activated electrodes after 15 CV cycles. b) Evolution of the non iR-corrected working potentials collected from the CV curves recorded using different PWs and measured at 100 mA cm^{-2}. c) The 15th CV scans shown in panel (a) for PWs1-3, focusing on current densities < 1 mA cm^{-2}. Measurement parameters/conditions: 5 mV s^{-1} in 1 M NaOH at RT.

≈0.38 $V_{Hg/HgO}$ prior to Ni(II) oxidation before the occurrence of OER. Moreover, the peak positions recorded on SSM316_PW3 have shifted anodically compared to those of pure $Ni(OH)_2$ deposited on glassy carbon (see Figure S3, Supporting Information). This peak anodic shift indicates the incorporation of Fe within the Ni species undergoing the Ni(II)→Ni(III) conversion prior to the OER.[37–39] Overall, this electrochemical characterization reveals that OER active species on the SSM316_PW3 surface are Fe-incorporated NiOOH, hereafter indicated as Ni(Fe)OOH. We should acknowledge the possibility that other metallic species present in SSM316 (e.g., Cr) may also influence the OER process (see our discussion on the role of Cr in Note S1, Supporting Information).[40]

In contrast to the SSM316_PW1 or SSM316_PW2 counterparts, the SSM316_PW3 electrode exhibited a greater amount of active species for the OER, as indicated by the integrated area of the reduction peak for Ni(III)→Ni(II) conversion (see Figure S4, Supporting Information). The measurements of their electrochemical active surface area (ECSA) also demonstrated that the SSM316_PW3 electrode has a larger ECSA value than SSM316_PW1 (Figure S5, Supporting Information). The efficient formation of Ni-based catalytic species on the SSM316_PW3 surface is associated to the more effective leaching of Fe compared to SSM316_PW1 and SSM316_PW2. This conclusion is experimentally supported by ICP-OES measurements conducted on the electrolytes used for activation procedures (Figures S6 and S7, Supporting Information), as well as by EDS data measured for the investigated electrodes (Table S1, Supporting Information). The leaching of Fe leads to the progressive surface exposure of Ni and Cr species, as evidenced by the appearance of an additional broad oxidation peak associated with Cr(III)→Cr(VI) at ≈0.38 $V_{Hg/HgO}$.[40] Importantly, in alkaline media, Cr (VI) is found in the form of dissolved $CrO_4{}^{2-}$,[41] as proved by monitoring Cr leaching through ICP measurements of the electrolyte (Figures S6 and S7, Supporting Information). The anodic leaching of Cr species has been previously reported as an effective route to improve the overall catalytic activity of SS electrode by creating a high-purity NiFe catalyst layer.[42] Also, the Ni(0)→$Ni(OH)_2$ oxidation process was previously reported to occur at ≈–0.6 V vs Hg/HgO, 1 M KOH[43] or ≈0.3 V_{RHE},[44] even though data in Figure 1c and Figure S3 (Supporting Information) indicate that oxidation currents observed in SSM316_PW3 near this potential window are mainly associated to the Fe(II)→Fe(III) conversion process.

To gain a deeper understanding on the effect of using PW3 to activate SSM316 for the OER, we conducted the following series of CV scans, varying PWs. Initially, a freshly cleaned SSM316 electrode was activated using 15 CV cycles with the PW3, resulting in the SSM316_PW3 electrode. Subsequently, this electrode underwent sequential CV measurements (labeled from 1 to 7). As illustrated in **Figure** 2a,b, the OER performances of the SSM316_PW3 slightly improved during the 2nd CV cycle, acquired using a PW of –1 to 1 $V_{Hg/HgO}$ (curve 2 vs curve 1). Beside this slight improvement of the OER activity, the oxidation peak of Cr(III)→Cr(VI) was still observed at ≈0.38 $V_{Hg/HgO}$. The 2nd CV scan stopped when potential returned to 0 $V_{Hg/HgO}$, and then the 3rd CV scan started from 0 $V_{Hg/HgO}$ (and stopped when scanned backward to 0 $V_{Hg/HgO}$. Notably, the 3rd CV scan showed a decreased OER performance (curve 3 vs curve 2), accompanied by the absence of the Cr(III)→Cr(VI) peak. Interestingly, the subsequent 4th scan, starting from 0 $V_{Hg/HgO}$ and scanning down to –1 $V_{Hg/HgO}$ and then up to 1 $V_{Hg/HgO}$ to finally return to 0 $V_{Hg/HgO}$, recovered the Cr(III)→Cr(VI) peak with a concomitant improvement of OER performance (curve 4 vs curve 3). As expected, the following CV scan encompassing the entire PW3 range maintained both the OER performance and the Cr(III)→Cr(VI) oxidation peak (curve 5 vs curve 4). In contrast, the subsequent two CV cycles conducted in the 0–1 $V_{Hg/HgO}$ (PW1 range) lost the Cr(III) →Cr(VI) oxidation peak while weakening the OER performance at the 7th CV scan (curve 7 vs curve 6), as the 6th CV scan was still influenced by the previous CV cycle with PW3.

Control experiments were additionally carried out on the SSM316_PW1 (Figure S8, Supporting Information), where the Cr(III)→Cr(VI) oxidation peak appeared when the PW1 was extended to PW3, increasing the OER activity. Based on the above results, we can conclude the following: 1) the incorporation of the –1 to –0.5 $V_{Hg/HgO}$ region within PW3 leads to the appearance of the Cr(III)→Cr(VI) oxidation peak, which diminishes if CV cycling is switched to the PW1; 2) CV cycles covering the –1 to –0.5 $V_{Hg/HgO}$ potential region, e.g., using the PW3 improves the OER activity of SSM316 cycled using 0–1 $V_{Hg/HgO}$ (PW1) range; 3) the disappearance of the Cr(III)→Cr(VI) oxidation peak is

© 2024 The Author(s). Advanced Materials published by Wiley-VCH GmbH

15214095, 2024, 21, Downloaded from https://onlinelibrary.wiley.com/doi/10.1002/adma.202312071 by Iit Istituti Italiano Di Tecnologia, Wiley Online Library on [27/09/2024]. See the Terms and Conditions (https://onlinelibrary.wiley.com/terms-and-conditions) on Wiley Online Library for rules of use; OA articles are governed by the applicable Creative Commons License

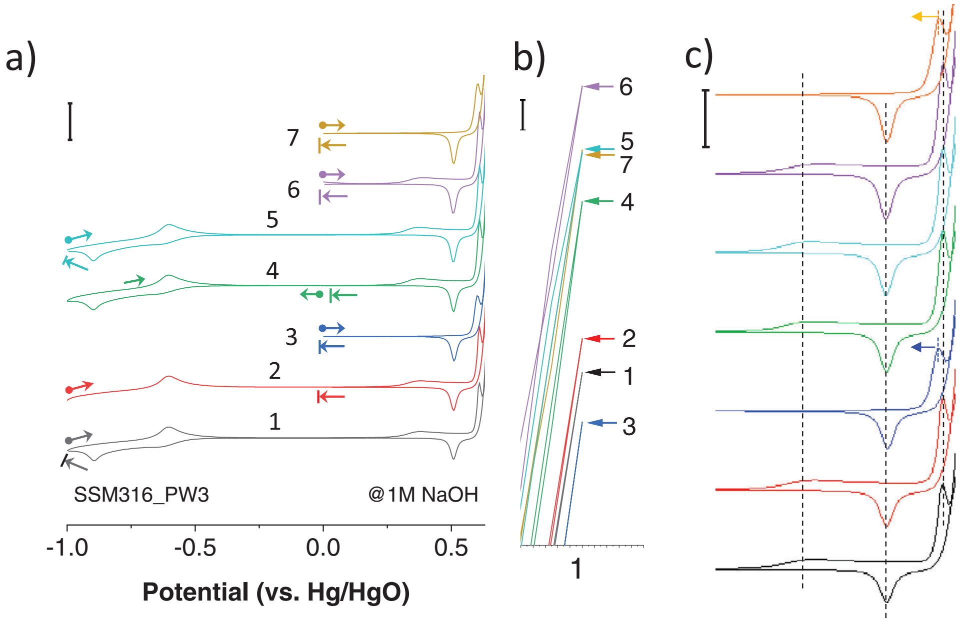

Figure 2. a) CV curves recorded for SSM316_PW3 at varying PWs. The arrow with the symbol "•" indicates the start of the scan, while the arrow with the symbol "I" indicates the end of the scan. b) Enlargement of the CV curves in the potential region ≈1 $V_{Hg/HgO}$ showing the maximum current density reached in each CV scan. c) Enlargement of the CV curves in the potential region showing the redox peaks prior to OER process. Scale bar: 1 mA cm^{-2}.

associated with a decrease of the OER activity. Considering that the Cr(III)→Cr(VI) oxidation peak appears when electrodes are scanned in PW covering the −1 $V_{Hg/HgO}$ to −0.5$V_{Hg/HgO}$ potential region (e.g., PW3), we speculate that the Cr(III)→Cr(VI) oxidation and the improved OER activity are linked to the occurrence of the Fe(II)↔Fe(III) redox process. In addition, the reduction of Ni(Fe)OOH species at potentials no lower than 0 $V_{Hg/HgO}$ is also the cause of surface deactivation.

Figure 2c reveals indeed that the oxidation peak position for Ni(II)→Ni(III) slightly shifts toward the cathodic direction when the Cr(III)→Cr(VI) oxidation disappears (as evident in curves 3 and 7 when the PW switched from PW3 to PW1). This peak shift evidences a decrease of the Fe content in the Ni(Fe)OOH species, likely caused by the reconstruction of the surface during the surface reduction at potentials no lower than 0 $V_{Hg/HgO}$.[37–39] Conversely, the Cr(III)→Cr(VI) peak reappears when cycling the electrodes with the PW3, and is accompanied by an anodic shift of the Ni(II)→Ni(III) peak position (as seen in curve 4 in Figure S8, Supporting Information). Figure S9 (Supporting Information) further supports the notion that the occurrence of the Cr(III)→Cr(VI) oxidation is correlated with the Fe(II)↔Fe(III) process. Overall, the Fe leaching exposes Cr and Ni species from the bulk structure of SSM316. The emerged Cr species are then oxidized at ≈0.38 $V_{Hg/HgO}$ and eventually dissolve as CrO_4^{2-}, while Ni species accumulate on the surface forming OER-active Ni(Fe)OOH species.

2.2. Spectral Characterizations and Analyses

SEM, X-ray diffraction (XRD) and X-ray photoelectron spectroscopy (XPS) measurements were carried out to elucidate the composition and chemical state of surface species on SSM316 before and after CV-aided activation with different PWs. As shown in Figure S10 (Supporting Information), SEM images indicated that the surface morphology of SSM316_PW1 after 15 CV cycles is identical to that of fresh (untreated) SSM316, while the SSM316_PW3 electrode after the same number of CV cycles exhibits slight corrosion on its surface. Such corrosion phenomenon becomes more evident after a higher number of CV cycles (35 cycles). XRD patterns recorded on SSM316 before and after CV-aided activation with the PW3 showed similar results to that of fresh SSM316 (Figure S11, Supporting Information). The absence of signals due to expected NiFe species is attributed to their low mass loading and their localization restricted to the only material surface. Thus, XPS was used to better evaluate chemical composition of the electrodes' surfaces.

As indicated in Figure S12 (Supporting Information), the surface of fresh SSM316 contains metallic Fe(0) and Ni(0) species, which oxidize after CV activation with both PW1 and PW3 (sample measured after stopping the CV cycling at 0 $V_{Hg/HgO}$). Interestingly, SSM316_PW1 shows more than 10 times lower Cr atomic content (at.%) (4.2 vs 32.3) and Fe/Ni at% (1.03 vs 12.8) compared to fresh SSM316 (Table S2, Supporting Information). As expected by the Cr Pourbaix diagram, the lower Cr content in SSM316_PW1 suggests that Cr is readily leached in the form of CrO_4^{2-} during the OER,[42] while the decrease of the Fe/Ni atomic ratio is associated with a faster corrosion of Fe compared to that of Ni, as also indicated by ICP (Figures S6 and S7, Supporting Information) and SEM-EDS (Table S1, Supporting Information) analyses. Notably, CV-aided activation of SSM316 with the PW3 ultimately results in the accumulation of Fe species at the electrode surface compared to SSM316_PW1, as evidenced by its significantly higher Fe/Ni atomic ratio (11.9 vs 1.03).

© 2024 The Author(s). Advanced Materials published by Wiley-VCH GmbH

15214095, 2024, 21, Downloaded from https://onlinelibrary.wiley.com/doi/10.1002/adma.202312071 by Iit Istituti Italiano Di Tecnologia, Wiley Online Library on [27/09/2024]. See the Terms and Conditions (https://onlinelibrary.wiley.com/terms-and-conditions) on Wiley Online Library for rules of use; OA articles are governed by the applicable Creative Commons License

15214095, 2024, 21, Downloaded from https://onlinelibrary.wiley.com/doi/10.1002/adma.202312071 by Iit Istituto Italiano Di Tecnologia, Wiley Online Library on [27/09/2024]. See the Terms and Conditions (https://onlinelibrary.wiley.com/terms-and-conditions) on Wiley Online Library for rules of use; OA articles are governed by the applicable Creative Commons License

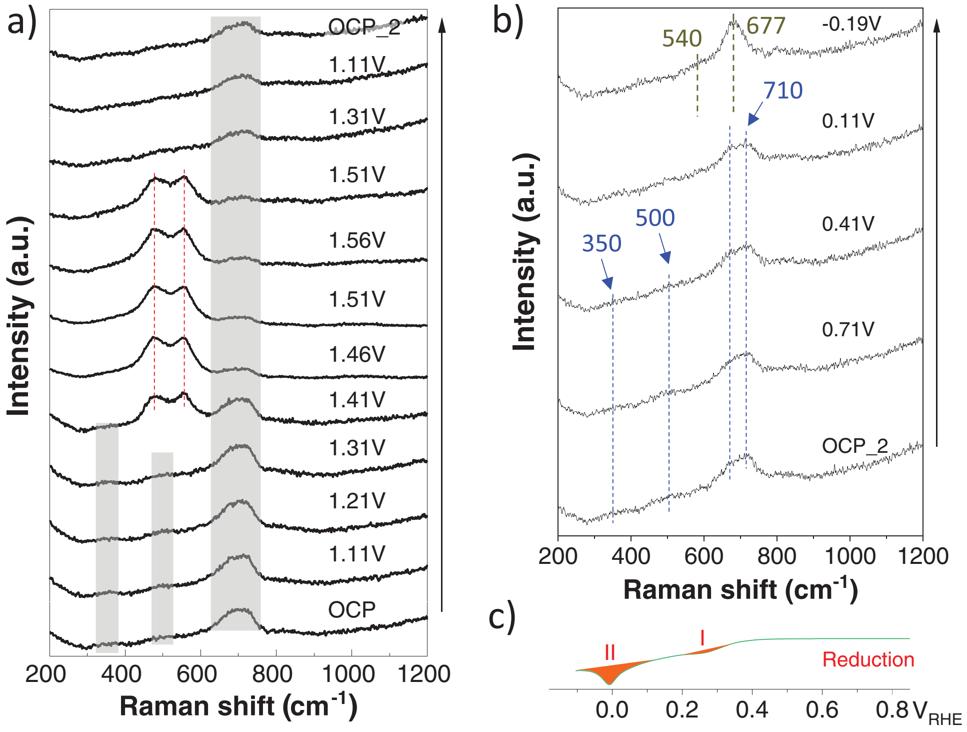

Figure 3. *Operando* Raman spectra recorded for SSM316_PW3 electrode as a function of the applied potential: a) from OCP to 1.56 V_{RHE}. The gray shadings indicate the peak areas expected for the γ-Fe_2O_3 species, while the red dashed lines denote the positions of Raman peaks of NiOOH species. b) From OCP to −0.19 V_{RHE}. The blue dashed lines indicate the Raman peaks of the γ-Fe_2O_3 species, while the olive dashed lines indicate the Raman peaks of Fe_3O_4 (and/or FeO). c) The cathodic part of the CV curve recorded on the same electrode considered in panel (b). I and II indicate two reduction peaks of Fe species.

Focusing on the chemical state of Fe species, the presence of satellite peaks at ≈719 and 733 eV indicates that both the SSM316_PW1 and SSM316_PW3 electrodes contain surface Fe(III) species, most likely in the form of FeOOH and/or Fe_2O_3[45] (for a more detailed discussion, refer to Figure S12, Supporting Information). Previous studies have shown that FeOOH can be transformed into Fe_2O_3 through a dehydration reaction,[46] jeopardizing the determination of the actual FeOOH/Fe_2O_3 content ratio in the operating catalysts. Further differentiating these Fe(III) species based solely on their XPS spectra is challenging, as different phases of Fe(III) (α-Fe_2O_3, γ-Fe_2O_3, etc.) show very similar spectra and closely spaced peak positions[45,47,48] To overcome these limits, Raman spectroscopy is an effective tool to identify Fe-based material phases.[49] As illustrated in Figure S13 (Supporting Information), Raman spectra obtained from two different areas of SSM316_PW3 consistently exhibit a prominent main peak at ≈710 cm^{-1}, which is the characteristic spectral feature of γ-Fe_2O_3.[50–52]

Regarding the Ni species (Figure S12b, Supporting Information), the XPS spectra of both SSM316_PW1 and SSM316_PW3 electrodes are similar and a good fitting of the data might be obtained in both cases with the set of peaks reported in literature for $Ni(OH)_2$.[53] The Raman features of Ni species are not observable, possibly due to the low content of Ni at the SSM316_PW3 surface, as supported by the aforementioned XPS results. Nevertheless, the Raman peaks of Ni species can emerge once $Ni(OH)_2$ is converted to NiOOH during the OER. For this reason, *operando* Raman spectroscopy (see set-up in Figure S14, Supporting Information) was conducted on CV SSM316_PW3 to monitor the evolution of surface species as a function of the applied potential. This approach provides valuable real-time insights into the dynamic compositional evolution of the surface species during electrochemical processes.

As shown in **Figure** 3a, the Raman spectra of the SSM316_PW3 electrode under open circuit potential (OCP) and potentials ranging from 1.11 to 1.31 V_{RHE} were consistent with ex-situ results. In this potential condition, γ-Fe_2O_3 is the main phase of Fe species. Above 1.41 V_{RHE}, two additional prominent peaks emerge at 478 and 556 cm^{-1}. These peaks are attributed to NiOOH and indicate the occurrence of $Ni(OH)_2 \rightarrow NiOOH$ oxidation process.[39,54] These peaks become more pronounced as the potential increases up to 1.56 V, where the OER takes place. Interestingly, the intensity ratio of the peaks at 556 and 478 cm^{-1} (I_{556}/I_{478}) is close to 1, suggesting a high structural disorder of the catalyst.[54–56] This may be attributed to the incorporation of Fe within the NiOOH host, as an I_{556}/I_{478} of only ≈0.8 was reported in the case of pure NiOOH.[54] Additionally, when the potential was lowered down to 1.11 V_{RHE}. NiOOH was reduced to $Ni(OH)_2$, as indicated by the absence of the characteristic Raman peaks of the former. Furthermore, Raman spectra were also recorded to investigate the Fe(III)→Fe(II) reduction process. As shown in Figure 3b, the Raman spectra profiles remained the same as that recorded at OCP conditions when the potential was decreased from

© 2024 The Author(s). Advanced Materials published by Wiley-VCH GmbH

0.71 to 0.11 V_{RHE}, indicating the presence of γ-Fe_2O_3. However, the main peak located at 710 cm^{-1} disappeared at −0.19 V_{RHE}, accompanied by the emergence of a new strong peak at ≈677 cm^{-1} and a shoulder peak at ≈540 cm^{-1}. These peaks can be attributed to Fe_3O_4 and/or FeO species.[51] The corresponding reduction part of the CV profile in Figure 3b also reveals the Fe(III)→Fe(II) reduction process (peak II) when scanned from positive to negative potentials (Figure 3c). Therefore, it can be concluded that the Fe_2O_3 on the surface of the SSM316_PW3 electrode is reduced to Fe_3O_4 (and/or FeO) at potentials below 0.1 V_{RHE}. Further distinguishing between Fe_3O_4 and FeO species is challenging as they exhibit identical Raman spectra. Our findings are consistent with previous reports, where magnetite Fe_3O_4 was observed as an intermediate species duringFe_2O_3 electroreduction[57,58] and a dissolution of $Fe_3O_4 \rightarrow Fe(OH)_3^-$ (aq.) was proposed in alkaline media.[59–61] The latter process well explains the occurrence of Fe leaching during SSM316 activation with the PW3.

2.3. OER Performance Evaluation of Activated SS electrodes

The successful activation strategy based on CV cycling with the PW3 was extended to other grades of commercially available SSs, namely, SSM304 and SSF316L. As expected, electrodes activated with the PW3 exhibited superior OER activity compared to those activated with the PW1, regardless of SS grade (Figures S15 and S16, Supporting Information). These results demonstrate the versatility of the proposed electrochemical activation approach for SS electrodes. The SSF316L electrode activated with the PW3 at room temperature in 1 M NaOH (named SSF316L_PW3) demonstrated the highest OER activity among the investigated SS electrodes, reaching 10 or 100 mA cm^{-2} at 0.62 or 0.655 $V_{Hg/HgO}$ (equal to 1.50 or 1.535 V_{RHE}). This performance positions SSF316L_PW3 as a promising electrolyzer anode, outperforming not only the commonly available electrodes in the market (e.g., Ni foam, $NiFeO_x$@Ti felt), but also the benchmark RuO_2-coated Ni foam (RuO_2@Ni foam) (Figure S17, Supporting Information), IrO_2-coated felt substrate (Figure S18, Supporting Information) and many previously reported OER electrocatalysts (Table S3, Supporting Information).

To investigate the activation of SS under different operation conditions for an alkaline electrolyzer, SSM316 was selected as a representative electrode, and the activation condition was switched from 1 M NaOH at room temperature (RT) to 6 M NaOH at either RT or 65 °C. As shown in Figure S19 (Supporting Information), compared to CV activation with PW3 in 1 M NaOH, the activation time (or number of cycles) of the electrode was greatly shortened in 6 M NaOH solution, while leading to higher OER activity tested in 1 M NaOH under RT (i.e., 0.67 V vs 0.685 $V_{Hg/HgO}$ at 100 mA cm^{-2}). Notably, further increasing the temperature of 6 M NaOH from RT to 65 °C did not result in a significant increase of the OER activity of the electrode (i.e., 0.66 V vs 0.67 $V_{Hg/HgO}$ at 100 mA cm^{-2}). This means that the activation process in highly concentrated alkaline solution at room temperature is already effective, without the need for thermal management systems to implement the activation procedure in-situ in practical systems, e.g., real electrolyzer. Eventually, we activated the SSM316 under a simulated industrial condition (30 wt.%, 80 °C) and further improved its activity (0.644 $V_{Hg/HgO}$ at 100 mA cm^{-2}).

Based on the knowledge acquired by the previous experiments, a potential-pulse protocol was developed to progressively restore the OER activity of SS electrodes over time, aiming at ensuring long-term performance in practical scenario. As illustrated in Figure S20 (Supporting Information), the SSM316 activated using the potential-pulse protocol, which switched the applied potential between 1 and −1 $V_{Hg/HgO}$, exhibited identical performance to that based on the CV protocol with the PW3. As shown in **Figure 4a**, two SSM316_PW3 replicas were tested controlling or not their operation through potential-pulse-based reactivation. More in detail, one electrode was operated continuously at 1 $V_{Hg/HgO}$. The other one was operated using a special potential-pulse protocol consisting of an operation at 1 $V_{Hg/HgO}$, intermittently switched to −1 $V_{Hg/HgO}$ for 2 min every 3 h. The results displayed that the potential-pulse protocol led to stable activity of SSM316_PW3 for over 300 h at ≈350 mA cm^{-2}. In comparison, the continuously operated SSM316_PW3 exhibited a significant current density decay of ≈37% after 250 h. Furthermore, their corresponding CV curves at low scan rate of 5 mV s^{-1} recorded before and after CA operation further revealed that the potential-pulse protocol retains and even slightly improves the OER activity after the stability test, while the continuous protocol resulted in a performance degradation (Figure 4b,c). SEM-EDS (Figure S21, Supporting Information) and XPS (Figure S22, Supporting Information) measurements both indicated that, compared to the SSM316 electrode after continuous test, additional Fe and Cr are leached after the potential-pulse test, exposing and accumulating more active species (Fe-incorporating NiOOH) at the SSM surface. This agrees with the enhanced OER activity observed for the SS electrodes treated through CV activation in the widest potential range of PW3. These findings highlight the effectiveness of the potential-pulse protocol in maintaining and even enhancing the OER activity of SS electrodes during practical operation.

The SS electrodes that were activated with the PW3 (generically denoted as SS_PW3) were coupled with a 40 wt.% Pt/C cathode (Pt mass loading = 0.4 mg cm^{-2}) to assemble alkaline water electrolyzer (AEL) single cell. The different single cell configurations are here denoted as anode‖cathode. The AELs were operated using 30 wt.% aqueous KOH as the electrolyte, and the cell was maintained at a temperature of 80 °C under atmospheric pressure (≈1 bar). The overall setup for the AEL test is illustrated in Figure 4d.

As optimized in previous works,[27,62,63] the anodes used in the investigated cells consisted of SSF316L_PW3 or stacked mesh-type electrodes SSM316_PW3 or SSM304_PW3. As indicated in the polarization curves acquired through chronopotentiometry measurements (Figure S23a,b, Supporting Information), the AEL based on SSF316L_PW3 showed slightly higher but comparable overpotentials compared to stacked SSM304_PW3 and SSM316_PW3. To assess the robustness of our SS anodes, the corresponding AELs were tested through a 24 h-accelerated stress test (AST) consisting of alternating galvanostatic steps between 1000 and 50 mA cm^{-2}, with each galvanostatic step kept for 15 min. The AEL based on SSF316L_PW3 demonstrated a lower performance durability compared to the other cases, with a significant increase of cell voltage at 1000 mA cm^{-2} by 112 mV during the AST. In contrast, the AELs based on SSM304_PW3 and SSM316_PW3 showed stable performances, i.e., the cell voltage increased only by 53.6and 32.7 mV, respectively (Figure 4e). The

© 2024 The Author(s). Advanced Materials published by Wiley-VCH GmbH

15214095, 2024, 21, Downloaded from https://onlinelibrary.wiley.com/doi/10.1002/adma.202312071 by Iit Istituto Italiano Di Tecnologia, Wiley Online Library on [27/09/2024]. See the Terms and Conditions (https://onlinelibrary.wiley.com/terms-and-conditions) on Wiley Online Library for rules of use; OA articles are governed by the applicable Creative Commons License

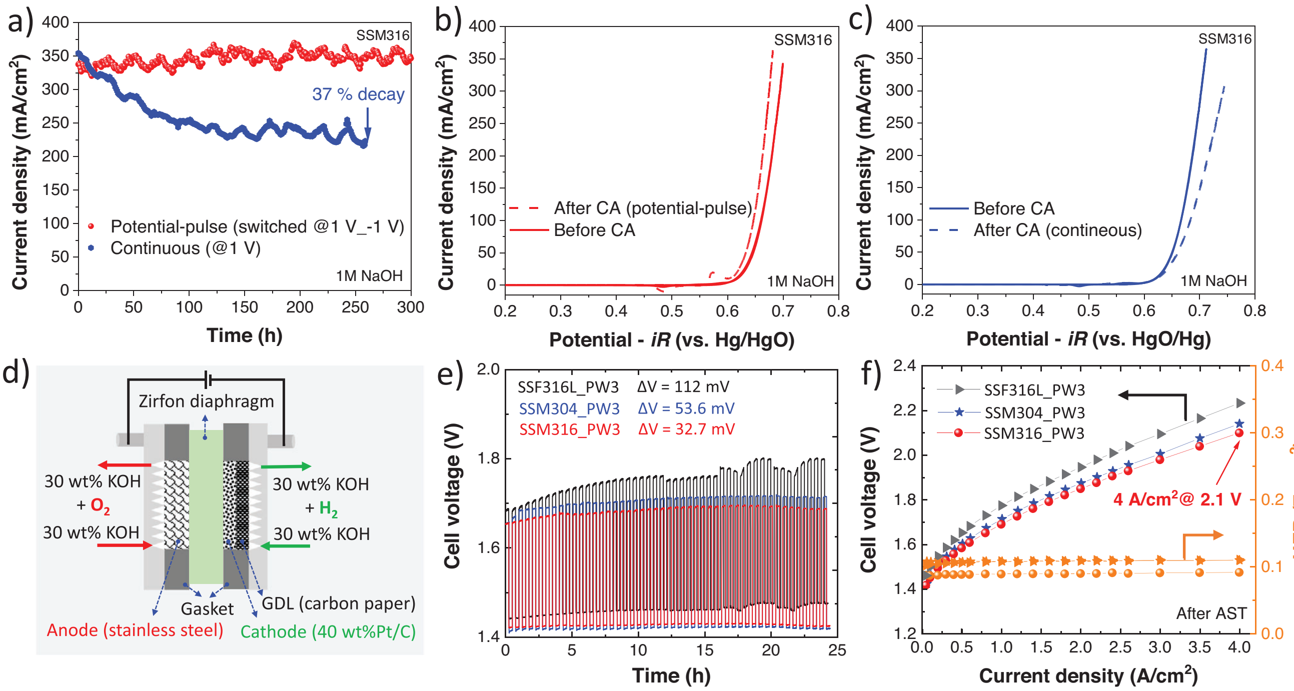

Figure 4. a) Chronoamperometric plots recorded on SSM316_PW3 using potential-pulse and continuous modes. The CV curves before and after stability tests using: b) potential-pulse and c) continuous modes. d) Sketch of the AEL single cell used in this work. e) AST measurement of the AEL single cells based on SS electrode activated with the PW3 as the anode and Pt/C cathode for 24 h. f) Non iR-corrected polarization curves measured for the investigated AEL single cells after the AST. Working conditions for AEL measurements: Zirfon Perl UTP 220 diaphragm; 30 wt.% KOH; 80 °C; 1 bar pressure. HFR: high frequency resistance.

durability trends observed during the ASTs were confirmed by comparing the CV curves measured for the investigated AELs before and after the ASTs (Figure S23d–f, Supporting Information). While the CV curve recorded for the AEL based on SSF316L_PW3 showed a significant increase of the polarizations, AELs based on SSM316_PW3 retained their initial performances, reaching current densities of 1000, 2000, and 4000 mA cm^{-2} at practical (non iR-corrected) cell voltages of 1.69, 1.85, and 2.1 V, respectively (Figure 4f). These values correspond to energy efficiencies (based on the hydrogen higher heating value) of 86.9%, 79.4%, and 69.9%, and can not only outperform those of electrolyzers based on a IrO_2 anode (Figure S24, Supporting Information) but also compete with the state-of-the-art ion-exchange membrane electrolyzers (Table S4, Supporting Information).

3. Conclusion

In summary, this study has investigated the effect of the potential window during the activation of SS electrodes for the OER by means of CV cycling. Using SSM316 as a representative SS electrode, we demonstrated that the voltammetric cycling from -1 to 1 $V_{Hg/HgO}$ (PW3) can significantly improve its OER activity compared to the cycling between 0 and 1 $V_{Hg/HgO}$. Thus, optimized CV-aided activated with PW3 decreases the overpotential to achieve 100 mA cm^{-2} by ≈40 mV compared to the other activation cases. Furthermore, a potential-pulse strategy was developed to periodically regenerate the OER activity of SS electrodes, leading to stable performances for over 300 h at current density as high as 350 mA cm^{-2} (whereas continuous mode operation caused a current density decay by 37%). Lastly, the optimally activated SS electrodes, including SSM316, SSM304, and SSF316L, were validated in practical AEL single-cell configurations. Our cells reached energy efficiency approaching state-of-the-art electrolyzers based on ion-exchange membrane, which, however, rely on Ir-based anodes (especially for proton-exchange membrane -PEM- electrolyzers, but also for anion-exchange membrane -AEM- electrolyzers) or display insufficient durability due to the mechanical and/or chemical instability of the membranes (especially for AEM electrolyzers). Prospectively, our potential-pulse strategy could be used to regenerate the performance of AELs, as well as other electrolyzer configurations, based on SS anodes and powered by intermittent electricity generated from energy sources such as solar and wind.

Supporting Information

Supporting Information is available from the Wiley Online Library or from the author.

Acknowledgements

This work has received funding from the European Union's Horizon 2020 "Proof of Concept" program under Grant Agreement No. 899412 (HyCat); the European Union's Horizon 2020 research and innovation program under Grant Agreement No. 881603- GrapheneCore3. The authors would like to thank Filippo Drago (Nanochemistry department – IIT) for the support in ICP analysis. The authors thank Dr. Michele Ferri for the discussion and assistance in *operando* Raman measurements. The authors also thank Dr. Francesco Bonaccorso, co-founder and CSO of BeDimensional S.p.A.

© 2024 The Author(s). Advanced Materials published by Wiley-VCH GmbH

15214095, 2024, 21, Downloaded from https://onlinelibrary.wiley.com/doi/10.1002/adma.202312071 by Iit Istituto Italiano Di Tecnologia, Wiley Online Library on [27/09/2024]. See the Terms and Conditions (https://onlinelibrary.wiley.com/terms-and-conditions) on Wiley Online Library for rules of use; OA articles are governed by the applicable Creative Commons License

Conflict of Interest

The authors declare no conflict of interest.

Data Availability Statement

Proper public repository will be indentified.

Keywords

activation, alkaline electrolyzer, oxygen evolution reaction, stainless steel

Received: November 13, 2023
Revised: February 8, 2024
Published online: March 1, 2024

[1] D. K. Bediako, Y. Surendranath, D. G. Nocera, *J. Am. Chem. Soc.* **2013**, *135*, 3662.
[2] Y. Zhou, S. Sun, C. Wei, Y. Sun, P. Xi, Z. Feng, Z. J. Xu, *Adv. Mater.* **2019**, *31*, 1902509.
[3] Y. Zuo, Y. Liu, J. Li, R. Du, X. Han, T. Zhang, J. Arbiol, N. J. Divins, J. Llorca, N. Guijarro, K. Sivula, A. Cabot, *Chem. Mater.* **2019**, *31*, 7732.
[4] H. Zhang, Y. Liu, T. Chen, J. Zhang, J. Zhang, X. W. Lou, *Adv. Mater.* **2019**, *31*, 1904548.
[5] O. Kasian, J. P. Grote, S. Geiger, S. Cherevko, K. J. J. Mayrhofer, *Angew. Chemie – Int. Ed.* **2018**, *57*, 2488.
[6] Z. P. Wu, X. F. Lu, S. Q. Zang, X. W. Lou, *Adv. Funct. Mater.* **2020**, *30*, 1910274.
[7] C. Roy, B. Sebok, S. B. Scott, E. M. Fiordaliso, J. E. Sørensen, A. Bodin, D. B. Trimarco, C. D. Damsgaard, P. C. K. Vesborg, O. Hansen, I. E. L. Stephens, J. Kibsgaard, I. Chorkendorff, *Nat. Catal.* **2018**, *1*, 820.
[8] C. C. L. McCrory, S. Jung, J. C. Peters, T. F. Jaramillo, *J. Am. Chem. Soc.* **2013**, *135*, 16977.
[9] F. Song, L. Bai, A. Moysiadou, S. Lee, C. Hu, L. Liardet, X. Hu, *J. Am. Chem. Soc.* **2018**, *140*, 7748.
[10] R. Chen, S. F. Hung, D. Zhou, J. Gao, C. Yang, H. Tao, H. Bin Yang, L. Zhang, L. Zhang, Q. Xiong, H. M. Chen, B. Liu, *Adv. Mater.* **2019**, *31*, 1903909.
[11] J. Zhang, L. Yu, Y. Chen, X. F. Lu, S. Gao, X. W. Lou, *Adv. Mater.* **2020**, *32*, 1906432.
[12] D. Friebel, M. W. Louie, M. Bajdich, K. E. Sanwald, Y. Cai, A. M. Wise, M. J. Cheng, D. Sokaras, T. C. Weng, R. Alonso-Mori, R. C. Davis, J. R. Bargar, J. K. Nørskov, A. Nilsson, A. T. Bell, *J. Am. Chem. Soc.* **2015**, *137*, 1305.
[13] J. Y. C. Chen, L. Dang, H. Liang, W. Bi, J. B. Gerken, S. Jin, E. E. Alp, S. S. Stahl, *J. Am. Chem. Soc.* **2015**, *137*, 15090.
[14] J. M. P. Martirez, E. A. Carter, *J. Am. Chem. Soc.* **2019**, *141*, 693.
[15] M. B. Stevens, C. D. M. Trang, L. J. Enman, J. Deng, S. W. Boettcher, *J. Am. Chem. Soc.* **2017**, *139*, 11361.
[16] Z. K. Goldsmith, A. K. Harshan, J. B. Gerken, M. Vörös, G. Galli, S. S. Stahl, S. Hammes-Schiffer, *Proc. Natl. Acad. Sci. USA* **2017**, *114*, 3050.
[17] M. Gorlin, J. F. De Araujo, H. Schmies, D. Bernsmeier, S. Dresp, M. Gliech, Z. Jusys, P. Chernev, R. Kraehnert, H. Dau, P. Strasser, *J. Am. Chem. Soc.* **2017**, *139*, 2070.
[18] M. Görlin, P. Chernev, J. F. De Araújo, T. Reier, S. Dresp, B. Paul, R. Krähnert, H. Dau, P. Strasser, *J. Am. Chem. Soc.* **2016**, *138*, 5603.
[19] B. J. Trześniewski, O. Diaz-Morales, D. A. Vermaas, A. Longo, W. Bras, M. T. M. Koper, W. A. Smith, *J. Am. Chem. Soc.* **2015**, *137*, 15112.
[20] R. D. L. Smith, C. Pasquini, S. Loos, P. Chernev, K. Klingan, P. Kubella, M. R. Mohammadi, D. González-Flores, H. Dau, *Energy Environ. Sci.* **2018**, *11*, 2476.
[21] B. M. Hunter, N. B. Thompson, A. M. Müller, G. R. Rossman, M. G. Hill, J. R. Winkler, H. B. Gray, *Joule* **2018**, *2*, 747.
[22] F. Moureaux, P. Stevens, G. Toussaint, M. Chatenet, *Appl. Catal. B* **2019**, *258*, 117963.
[23] B. Chen, A. L. G. Biancolli, C. L. Radford, S. Holdcroft, *ACS Energy Lett.* **2023**, *8*, 2661.
[24] Y. Liu, Z. Song, Z. Li, M. Han, Y. Cheng, Z. Zheng, *Catal. Commun.* **2022**, *164*, 106425.
[25] T. N. Pham, A. Samikannu, Z. Vincze, P. Zettinig, S. Tesfalidet, T. Wågberg, J.-P. Mikkola, T. N. Pham, A. Samikannu, S. Tesfalidet, J. Mikkola, Z. Vincze Entrepreneurship, P. Zettinig, *Adv. Sustain Syst.* **2022**, *6*, 2200310.
[26] W. Zhu, T. Zhang, Y. Zhang, Z. Yue, Y. Li, R. Wang, Y. Ji, X. Sun, J. Wang, *Appl. Catal. B* **2019**, *244*, 844.
[27] Y. Zuo, S. Bellani, M. Ferri, G. Saleh, D. V. Shinde, M. I. Zappia, R. Brescia, M. Prato, L. De Trizio, I. Infante, F. Bonaccorso, L. Manna, *Nat. Commun.* **2023**, *14*, 4680.
[28] X. Lyu, J. Li, C. J. Jafta, Y. Bai, C. P. Canales, F. Magnus, Á. S. Ingason, A. Serov, *J. Environ. Chem. Eng.* **2022**, *10*, 108486.
[29] X. Hu, X. Tian, Y. W. Lin, Z. Wang, *RSC Adv.* **2019**, *9*, 31563.
[30] F. Moureaux, P. Stevens, G. Toussaint, M. Chatenet, *J. Power Sources* **2013**, *229*, 123.
[31] H. Schäfer, S. Sadaf, L. Walder, K. Kuepper, S. Dinklage, J. Wollschläger, L. Schneider, M. Steinhart, J. Hardege, D. Daum, *Energy Environ. Sci.* **2015**, *8*, 2685.
[32] H. Schäfer, S. M. Beladi-Mousavi, L. Walder, J. Wollschläger, O. Kuschel, S. Ichilmann, S. Sadaf, M. Steinhart, K. Küpper, L. Schneider, *ACS Catal.* **2015**, *5*, 2671.
[33] A. Meena, P. Thangavel, D. S. Jeong, A. N. Singh, A. Jana, H. Im, D. A. Nguyen, K. S. Kim, *Appl. Catal. B* **2022**, *306*, 121127.
[34] S. Hao, H. Sheng, M. Liu, J. Huang, G. Zheng, F. Zhang, X. Liu, Z. Su, J. Hu, Y. Qian, L. Zhou, Y. He, B. Song, L. Lei, X. Zhang, S. Jin, *Nat. Nanotechnol.* **2021**, *16*, 1371.
[35] M. J. Jang, S. H. Yang, M. G. Park, J. Jeong, M. S. Cha, S. H. Shin, K. H. Lee, Z. Bai, Z. Chen, J. Y. Lee, S. M. Choi, *ACS Energy Lett.* **2022**, *7*, 2576.
[36] S. Loos, I. Zaharieva, P. Chernev, A. Lißner, H. Dau, *ChemSusChem* **2019**, *12*, 1966;
[37] L. Trotochaud, S. L. Young, J. K. Ranney, S. W. Boettcher, *J. Am. Chem. Soc.* **2014**, *136*, 6744.
[38] Z. Lu, W. Xu, W. Zhu, Q. Yang, X. Lei, J. Liu, Y. Li, X. Sun, X. Duan, *Chem. Commun.* **2014**, *50*, 6479.
[39] M. W. Louie, A. T. Bell, *J. Am. Chem. Soc.* **2013**, *135*, 12329.
[40] C. M. Abreu, M. J. Cristóbal, R. Losada, X. R. Nóvoa, G. Pena, M. C. Pérez, *Electrochim. Acta* **2006**, *51*, 2991.
[41] K. Huang, L. Wang, Y. Wen, K. He, M. Zhang, J. Du, X. Hu, *Front Chem* **2022**, *10*, 958773.
[42] S. Anantharaj, M. Venkatesh, A. S. Salunke, T. V. S. V. Simha, V. Prabu, S. Kundu, *ACS Sustainable Chem. Eng.* **2017**, *5*, 10072.
[43] A. Seghiouer, J. Chevalet, A. Barhoun, F. Lantelme, *J. Electroanal. Chem.* **1998**, *442*, 113.
[44] L. D. Burke, T. A. M. Twomey, *J. Electroanal. Chem.* **1984**, *162*, 101.
[45] M. C. Biesinger, B. P. Payne, A. P. Grosvenor, L. W. M. Lau, A. R. Gerson, R. S. C. Smart, *Appl. Surf. Sci.* **2011**, *257*, 2717.
[46] F. Watari, P. Delavignette, J. Van Landuty, S. Amelinckx, *J. Solid State Chem.* **1983**, *48*, 49.
[47] T. Yue, Z. Niu, H. Tao, X. He, W. Sun, Y. Hu, Z. Xu, *ACS Sustainable Chem. Eng.* **2019**, *7*, 6821.
[48] A. P. Grosvenor, B. A. Kobe, M. C. Biesinger, N. S. McIntyre, *Surf. Interface Anal.* **2004**, *36*, 1564.
[49] M. Hanesch, *Geophys. J. Int.* **2009**, *177*, 941.
[50] N. Boucherit, A. Hugot-Le Goff, S. Joiret, *Corros. Sci.* **1991**, *32*, 497.
[51] D. L. A. De Faria, S. Venâncio Silva, M. T. De Oliveira, *J. Raman Spectrosc.* **1997**, *28*, 873.

© 2024 The Author(s). Advanced Materials published by Wiley-VCH GmbH

15214095, 2024, 21, Downloaded from https://onlinelibrary.wiley.com/doi/10.1002/adma.202312071 by Iit Istituti Italiano Di Tecnologia, Wiley Online Library on [27/09/2024]. See the Terms and Conditions (https://onlinelibrary.wiley.com/terms-and-conditions) on Wiley Online Library for rules of use; OA articles are governed by the applicable Creative Commons License

[52] R. P. Morco, A. Y. Musa, M. Momeni, J. C. Wren, *Corros. Sci.* **2016**, *102*, 1.
[53] M. C. Biesinger, B. P. Payne, L. W. M. Lau, A. Gerson, R. S. C. Smart, *Surf. Interface Anal.* **2009**, *41*, 324.
[54] F. Bao, E. Kemppainen, I. Dorbandt, F. Xi, R. Bors, N. Maticiuc, R. Wenisch, R. Bagacki, C. Schary, U. Michalczik, P. Bogdanoff, I. Lauermann, R. Van De Krol, R. Schlatmann, S. Calnan, *ACS Catal.* **2021**, *11*, 10537.
[55] R. Y. Fan, H. Y. Zhao, Z. Y. Zhao, W. H. Hu, X. Liu, J. F. Yu, H. Hu, Y. M. Chai, B. Dong, *Nano Res.* **2022**, *1*.
[56] H. Liao, X. Zhang, S. Niu, P. Tan, K. Chen, Y. Liu, G. Wang, M. Liu, J. Pan, *Appl. Catal. B* **2022**, *307*, 121150.
[57] K. K. Lee, S. Deng, H. M. Fan, S. Mhaisalkar, H. R. Tan, E. S. Tok, K. P. Loh, W. S. Chin, C. H. Sow, *Nanoscale* **2012**, *4*, 2958.
[58] R. M. Cornell, U. Schwertmann, The Iron Oxides, Wiley-VCH Verlag GmbH & Co. KGaA, Weinheim **2003**, https://doi.org/10.1002/3527602097.
[59] P. D. Allen, G. J. Bignold, N. A. Hampson, *J. Electroanal. Chem.* **1980**, *112*, 239.
[60] A. Allanore, H. Lavelaine, G. Valentin, J. P. Birat, P. Delcroix, F. Lapicque, *Electrochim. Acta* **2010**, *55*, 4007.
[61] Y. A. Ivanova, J. F. Monteiro, L. B. Teixeira, N. Vitorino, A. V. Kovalevsky, J. R. Frade, *Mater. Des.* **2017**, *122*, 307.
[62] Y. Zuo, S. Bellani, G. Saleh, M. Ferri, D. V. Shinde, M. I. Zappia, J. Buha, R. Brescia, M. Prato, R. Pascazio, A. Annamalai, D. O. de Souza, L. De Trizio, I. Infante, F. Bonaccorso, L. Manna, *J. Am. Chem. Soc.* **2023**, *145*, 21419.
[63] M. I. Zappia, S. Bellani, Y. Zuo, M. Ferri, F. Drago, L. Manna, F. Bonaccorso, *Front Chem* **2022**, *10*, 1045212.

15214095, 2024, 21, Downloaded from https://onlinelibrary.wiley.com/doi/10.1002/adma.202312071 by Iit Istituti Italiano Di Tecnologia, Wiley Online Library on [27/09/2024]. See the Terms and Conditions (https://onlinelibrary.wiley.com/terms-and-conditions) on Wiley Online Library for rules of use; OA articles are governed by the applicable Creative Commons License

© 2024 The Author(s). Advanced Materials published by Wiley-VCH GmbH